



HAL
open science

From surface fault traces to a fault growth model: the Vogar fissure swarm of the Reykjanes Peninsula, Southwest Iceland

Thierry Villemin, Françoise Bergerat

► **To cite this version:**

Thierry Villemin, Françoise Bergerat. From surface fault traces to a fault growth model: the Vogar fissure swarm of the Reykjanes Peninsula, Southwest Iceland. *Journal of Structural Geology*, 2013, pp.1-35. 10.1016/j.jsg.2013.03.010 . hal-00815189

HAL Id: hal-00815189

<https://hal.science/hal-00815189v1>

Submitted on 19 Apr 2013

HAL is a multi-disciplinary open access archive for the deposit and dissemination of scientific research documents, whether they are published or not. The documents may come from teaching and research institutions in France or abroad, or from public or private research centers.

L'archive ouverte pluridisciplinaire **HAL**, est destinée au dépôt et à la diffusion de documents scientifiques de niveau recherche, publiés ou non, émanant des établissements d'enseignement et de recherche français ou étrangers, des laboratoires publics ou privés.

1 **From surface fault traces to a fault growth model: the Vogar Fissure Swarm of the**
2 **Reykjanes Peninsula, Southwest Iceland.**

3

4 **Thierry Villemin^a, Françoise Bergerat^b ***

5 ^a EDYTEM (UMR 5204 CNRS-Université de Savoie), Campus scientifique, 73376 Le
6 Bourget du lac Cedex, France - Thierry.Villemin@univ-savoie.fr

7 ^b IStEP (UMR 7193 CNRS-UPMC), Université Pierre et Marie Curie, Case 117, 4, Place
8 Jussieu, 75252 Paris Cedex 05, France - Francoise.bergerat@upmc.fr - Tel. 33 1 44 27 34 43

9

10 **Keywords**

11 Icelandic rift, Fissure swarm, Normal fault growth, Remote sensing, Photogrammetric
12 techniques, Divergent plate boundary.

13

14 **Abstract**

15 The Vogar Fissure Swarm is one of four en-echelon fracture swarms that connect the
16 Reykjanes Ridge to the South Iceland Seismic Zone and the Western Volcanic Zone.
17 Occurring in an area of flat topography, this fissure swarm is clearly visible at the surface,
18 where it can be seen to affect recent postglacial lavas. Using remote sensing methods to
19 identify and measure all the faults and fractures in the swarm, combined with additional field
20 observations and measurements, we measured 478 individual fractures, 33% of them being
21 faults and 67% being fissures. The fracture lengths show roughly log-normal distributions.
22 Most of the individual fractures belong to 68 main composite fractures, seven of which are
23 longer than 2500 m and correspond to the main fault scarps of the fissure swarm. We showed
24 that these main faults are distributed along five, equally spaced zones, ~500 m apart and a few
25 kilometers long. We drawn 71 across-strike profiles to characterize the shape of the fault
26 scarps, and 5 along-strike profiles to characterize the evolution of vertical throw along the
27 main faults. Each fault consists of a coalescence of individual segments of approximately
28 equal length. Fault throws are never larger than 10 m and are smallest at the junctions
29 between individual segments. Analyses of along-strike throw profiles allowed us to determine
30 the early stages of growth after coalescence. The earliest stage is characterized by an increase

31 in the throw of the central parts of segments. This is followed by a second stage during which
32 the throw increases at the junctions between segments, progressively erasing these small-
33 throw zones.

34 **1. Introduction**

35 Iceland's neovolcanic rift zone is the surface expression of the mid-Atlantic plate
36 boundary. It consists of three main segments, known as the Northern, Eastern and Western
37 Volcanic Zones, which are linked to the Kolbeinsey Ridge to the north and the Reykjanes
38 Ridge to the south (Fig. 1A). Southern Iceland's Reykjanes Peninsula lies between the
39 Western Volcanic Zone and the offshore Reykjanes Ridge, and includes features
40 characteristic of both divergent and transform-type plate boundaries. The general purpose of
41 the present research is to better understand fault growth at such divergent plate boundary. The
42 Vogar fissure swarm provides the most suitable conditions for this, as the structures are clear
43 on postglacial lava flows and not on loose terrain with vegetation.

44 The volcanic zones are crossed by what are generally referred to as fissure swarms
45 (Sæmundsson, 1978) and include central volcanoes, eruptive volcanic fissures, tension
46 fractures, and faults. Numerous studies have examined the fracture geometry of some of
47 Iceland's fissure swarms (Sæmundsson 1978, 1992; Guðmundsson, 1987b; Opheim and
48 Guðmundsson, 1989; Guðmundsson and Bäckström, 2000; Tentler and Mazzoli, 2005; Friese,
49 2008; Hjartardottir et al., 2009), and the main features of the Vogar Fissure Swarm have been
50 described as part of general studies of the Reykjanes Peninsula (Guðmundsson, 1980, 1986,
51 1987a; Grant and Kattenhorn, 2004; Clifton and Kattenhorn, 2006). Other research has shown
52 that detailed topographical analyses of fissure swarms can be used to determine the geometry
53 and mechanical behavior of the underlying extensional structure (Guðmundsson, 1992;
54 Angelier et al. 1997; Dauteuil et al., 2001, Acocella et al., 2003).

55 Investigations of the spatial distribution of faults and fissures are essential for
56 understanding the mechanisms underlying fault growth, and, more generally, brittle failure
57 behaviors (Cowie et al., 1996; Torabi and Berg, 2011). Linkage and forward propagation
58 models can be used to explain field observations. How fault segments coalesce and how this
59 coalescence produces changes in fault architecture have been particularly well documented in
60 different rock types and in different tectonic settings. Numerous studies have analyzed either
61 surface (horizontal) faulting configurations (e.g., Peacock, 1991; Cartwright et al., 1995;
62 Childs et al., 1995; Huggins et al., 1995) or vertical faulting configurations (e.g., Peacock and
63 Zhang, 1993; Childs et al., 1996; Mansfield and Cartwright, 1996; Schöpfer et al., 2006). In

64 fact, linkages between the different parts of normal faults occur both vertically and
65 horizontally, and on a broad range of scales. Despite all these studies, some aspects of fault
66 initiation and development are still poorly understood and subject to debate.

67 The aims of the present work were thus: (1) to produce a detailed description of the
68 structure of the Vogar Fissure Swarm (Fig. 1C) as the basis for an analysis of its fracture style
69 and behavior, and (2) to draw up a 3D tectonic model for the formation and growth of normal
70 faulting in this type of fissure swarm characteristic of the Icelandic divergent boundary. To do
71 this we combined (i) remote mapping based on geo-referencing, orthorectification, and 3D
72 photogrammetric restitution of aerial photographs with (ii) geodetic (GPS) ground control
73 points and (iii) field observations and measurements taken to check the remote data. The
74 resulting accurate map of the Vogar Fissure Swarm allowed us to analyze the layout and
75 throws of the normal faults in three dimensions and at a level of detail not previously attained
76 for this size area. We (i) determined the type, length, and spacing of 478 individual
77 decameter- to kilometer-scale fractures, (ii) characterized the shape of the fault scarps in 71
78 across-strike profiles, and (iii) measured the along-strike evolution of vertical throw along
79 five main fault scarps.

80

81 **2. Geological setting**

82 The deformation in southwest Iceland is accommodated by three major structures: the
83 Reykjanes Peninsula (RP) to the south, the Western Volcanic Zone (WVZ) to the north and
84 the South Iceland Seismic Zone (SISZ) to the east (Fig. 1A). The direction of plate motion at
85 the 30°-trending Reykjanes Ridge (offshore segment of the Mid-Atlantic Ridge) to the south
86 of Iceland is N104° (DeMets, 1990, 1994). To the east, the SISZ is a major E-W left-lateral
87 transform zone that connects the RP to the Eastern Volcanic Zone (EVZ). However, part of
88 the extension continues along the WVZ. The RP is highly oblique to the direction of plate
89 motion and geodetic studies have shown that plate spreading is accommodated both by left
90 lateral shear (17-19 mm/yr) and by opening (7-9 mm/yr) below a locking depth of 6-9 km
91 (Árnadóttir et al., 2008; Keiding et al., 2009). Leveling measurements along profiles through
92 the RP indicate vertical displacement on normal faults of up to several millimeters over a
93 period of about ten years, together with regional tilting (Tryggvason, 1974, 1982).

94 The divergent plate boundary in the RP runs for 70 km between Hengill volcano to the
95 north and the tip of the peninsula to the south, and has an overall trend of ~70°. It consists of

96 four main en-echelon fissure swarms, trending $\sim 45^\circ$. From west to east, these swarms are the
97 Reykjanes, Krýsuvík, Bláfjöll, and Hengill swarms (Fig. 1B).

98 The Reykjanes Fissure Swarm is a 35 km by 5-8 km zone of recent faulting, fissuring
99 and volcanism that is directly connected to the offshore Reykjanes Ridge to the south.
100 Onshore, it extends from the northern coast of the RP to its southwestern tip (Fig. 1C), cutting
101 through postglacial basaltic pahoehoe lavas older than AD 871 and younger than 0.8 My. Its
102 northern part, called the Vogar Fissure Swarm (VFS), is separated from its southern part by aa
103 lavas younger than AD 871 (Jóhannesson and Sæmundsson, 2009).

104 The VFS (Fig. 1C) clearly shows the recent fracture pattern, allowing it to be
105 geometrically analyzed over a wide range of scales, from minor fissures to large fault-tilted
106 blocks.

107

108 **3. Methodology**

109 We used 1:25,000 scale aerial photographs obtained from “Landmælingar Íslands”
110 (Geographic Survey of Iceland) to map the fractures of the VFS and analyze their number,
111 length, density, and throws. These photos, which covered an area of approximately 30 km²,
112 were digitized at a resolution of 1200 dpi (i.e. a ground resolution of 0.5 m). The main data
113 acquisition stages involved building a mosaic of aerial photographs and carrying out
114 stereoscopic analyses of photographic pairs. Additional detailed observations and
115 measurements were made using photographs taken from a helicopter.

116 We used ErMapper® software to spatially register and rectify the photographs with
117 respect to Ground Control Points (GCP) and to a Digital Elevation Model (DEM) of the area
118 at a resolution of one point every 90 m. GCP coordinates were measured using GPS mono-
119 frequency Trimble receivers and GPS data were analyzed using Pathfinder Office® software.
120 Mean calculated errors were 2-5 cm (horizontal) and 5-10 cm (vertical), so measurement
121 uncertainties were negligible compared with the measurement errors the irregular texture of
122 the lava flows would induce in ordinary field observations. Following orthorectification of
123 each photograph, we created a mosaic for the whole study area (Fig. 2), which we then used
124 as a base map for plotting the fracture traces, added using Autocad Map®.

125 Stereo-photographic pairs were constructed in line with the principles of parallel
126 stereoscopy (Kasser and Egels, 2001) and using the Poivilliers software developed by Yves
127 Egels at France’s National Geographic Institute. Overlaps between two adjacent photographs

128 were ~60%. The process involved two main steps: (i) creation of photogrammetric models
129 and (ii) use of these models to characterize the types of fracture and to measure scarp heights,
130 which can be considered to represent the vertical throws of the faults, as erosion is negligible
131 in Holocene lava flows.

132 Each stereo pair was constructed using interior and absolute (exterior) orientation
133 parameters. When constructing stereo pairs in this way, interior orientation requires that
134 camera fiducial marks are positioned independently for each photograph, so the location of
135 the principal point (projection of the perspective center on the image plane) can be calculated.
136 We then identified several tie points and GCPs on both photographs of a stereo pair in order
137 to simultaneously obtain relative and absolute orientations. Each point was identified by its
138 coordinates on both the left (x_l, y_l) and right (x_r, y_r) images. This step is based on co-linearity
139 and straight-line co-planarity conditions (Kasser and Egels, 2001). At least three GCPs spread
140 across the entire stereo pair and at least five tie points are needed to determine absolute
141 orientations. We used ground coordinates from GPS benchmarks as GCPs. The accuracy of
142 our photogrammetric models enabled us to determine 3D coordinates for each point with
143 horizontal and vertical precisions of 0.5 m. The lava flows have such uneven surfaces that
144 altitude differences of less than 0.5 m are not significant (Guðmundsson, 1992).

145 This process allowed us to identify and position each fracture in three dimensions, and
146 to plot the fractures on the mosaic, using different colors to depict throw and opening
147 characteristics (Fig. 2). The resulting fracture map was used to analyze the geometry of
148 individual fracture traces within the VFS. We did not do any mapping in the Skógfellahraun
149 aa lava flow (Fig. 2) because of the difficulty of following (and measuring) fracture traces in
150 these very friable and jumbled lavas.

151 We used the stereo pairs to draw along-strike topographic profiles of the footwalls and
152 hanging walls of five main fracture lines over a distance of 14 km. We obtained 20
153 topographic profiles by drawing four profiles for each fracture line, two on the hanging wall
154 and two on the footwall, at distances of 20 m and 40 m from the main scarp. We then used
155 these topographic profiles, interpolating where necessary to obtain the points needed for
156 calculating differences in elevation between the hanging wall and the footwall for each
157 fracture line (see Fig. 10, section 4.6).

158 Moreover, punctual field observations and measurements have been carried out as
159 control points to validate the mapping of fractures and the profile values.

160

161 **4. Results**

162 The following descriptions of the geometrical characteristics of the fracturing are
163 based on data obtained by analyzing aerial photographs as described above, combined with
164 field observations and measurements.

165 *4.1 Fracture type terminology*

166 We produced maps of the VFS by tracing features from stereoscopic aerial
167 photographs. The term “fracture” is used hereafter to refer to all types of mechanical
168 discontinuity with a tectonic origin. We differentiated two types of fracture, those with
169 vertical throw, referred to as normal faults, and those without vertical throw (or with vertical
170 throw smaller than 0.5 m which corresponds to the accuracy obtained by the photogrammetric
171 model), referred to as fissures. Some normal faults were open, others were not (Fig. 6). The
172 normal faults in the VFS are actually vertical faults with both vertical displacement and
173 dilation (Fig. 5). The Icelandic names for the main fault scarps, which also have a significant
174 dilation component, end in “gjá” (Fig. 2), which means gap. These faults become true normal
175 faults (shear) at depth (e.g., Angelier et al., 1997).

176 We refer to fractures that can be traced continuously as “individual fractures”.
177 Individual fractures commonly concentrate in fracture strips that may be discontinuous and
178 are of varying lengths. Most fracture strips, which we refer to as “main composite fractures”
179 (Fig. 3), are composed of several aligned individual fractures, generally including both
180 fissures and faults (Fig. 2). For mapping purposes, we considered parallel main composite
181 fractures to be separate if they are more than 125 m apart and aligned main composite
182 fractures to be separate if they are more than 250 m apart.

183 One difficulty with this type of mapping is the difference between the scale of the
184 photographs and the scale of the map. At the scale of the photographs used for our study, two
185 small lines close together may be indistinguishable and appear as a single line, whereas they
186 would appear as two separate lines on a more detailed photograph or in the field. In addition,
187 some large fracture lines may be quite thick due to the coalescence of several individual but
188 indistinguishable fractures.

189 *4.2 Number of fractures and organization of the network*

190 We mapped 478 individual fractures (a few were only partially mapped because of the
191 presence of the aa lava flow) in the study area (Fig. 2), 33% of which are normal faults and
192 67% are fissures. Most belong to the 68 main composite fractures (Fig. 3), seven of which are
193 more than 2500 m long and correspond to the main fault scarps of the fissure swarm (Fig. 4).

194 Except close to the Skógfellahraun aa lava flow, the main composite fractures in the
195 western part of the VFS are composed mostly of fissures, whereas those in its eastern part are
196 composed mostly of normal faults. The VFS is ~10 km long, measured from the aa lava flow
197 to its northeastern tip, and tapers from ~4.5 km wide close to the aa lava flow to ~3 km wide
198 at its northeastern tip.

199 The western edge of the VFS is formed by a major, east-facing normal fault, called
200 Hrafnagjá (Fig. 2; R16 in Fig. 3), whereas its eastern edge is formed by a series of open
201 fissures, called Brunnastaðaselsgjá (Fig. 2; R66-67 in Fig. 3). The area between these two
202 boundaries contains five major west-facing normal faults in a step pattern (Fig. 2). The
203 easternmost major normal fault scarp is called Grindavikurgjá (Fig. 2; R59 in Fig. 3).
204 Individual fracture strikes (fissures and faults), based on their mean linear orientation
205 weighted by the length of each fracture segment, are between N30°E and N70°E, with a mean
206 strike of N55-60°E (Fig. 3).

207 *4.3 Length and density*

208 The main composite fractures are between 250 m and 5.6 km long (Fig. 7 C).
209 Individual faults are between 34 and 1288 m long (mean length 229 m). Individual fissures
210 have a comparable minimum length (23 m) but maximum and average lengths are
211 significantly shorter (545 m and 139 m, respectively). Because the aa lava flows
212 (southwestern part of Fig. 2) prevented us fully mapping a crucial part of the faults, their
213 mean and maximum lengths were almost certainly underestimated. This is only a minor
214 problem for the fissuring. However, some of the shortest fissures (<10 m) are probably
215 masked by soil and grass, so this class is likely to be under-represented. What is more, these
216 small fissures are similar in size to non-tectonic, cooling fractures in the lavas, so it was not
217 always possible to measure them.

218 The length distributions of all the sets of fractures (Fig. 7 A and B) show roughly log-
219 normal distributions (“heavy tail” type); therefore, the average length is not characteristic.
220 Consequently, the classes with the highest frequencies are [75-100 m] for the faults and [50-
221 100 m] for the fissures.

222 The cumulative lengths of all the fractures mapped were 44.9 km for the fissures and
223 35.7 km for the faults, which gives fracture densities for the area affected by faulting of 1.45
224 m/m^2 and $1.15 \text{ m}/\text{m}^2$, respectively.

225 *4.4 Spacing*

226 We measured the spacing between the fractures in the VFS along profiles
227 perpendicular to the maximum frequency directions indicated by the rose diagrams (Fig. 3).
228 Profile lengths (distance between most northwesterly and most southeasterly fractures) were
229 between 1700 m and 4100 m. The linear density of fractures (number of fractures per unit
230 length) depends on the type of fracture:

231 - The density of the fissures is extremely variable, depending on where the cross-
232 section was taken. The spacing distribution shows modes at 75 m, 225 m, and 450 m (Fig. 8).
233 There are probably modes at other multiples but these modes are difficult to determine due to
234 the limited number of sampling values. These multiples result from the non-persistence of the
235 fissures.

236 - The spacing distribution for all the individual fractures (faults and fissures) also
237 shows modes at 75 m, 225 m, and 450 m (Fig. 8). Some multiples may be less visible because
238 fractures do not necessarily extend across the entire study area. Fissures linking two segments
239 of a fault, thereby making the combined fissure longer, are very common.

240 - The spacing distribution of the composite fractures shows only two modes, at 225 m
241 and 450 m (Fig. 8). The mode at 75 m is not present because fractures that are less than 125 m
242 apart were shown by a single line when we drew the composite fractures map.

243 The three modes noted above can be seen clearly in Figures 2 and 3. Their significance
244 is discussed in section 5.

245 *4.5 Topography of the fissure swarm and across-strike throws*

246 Using the automatic protocol described in section 3, we drew 71 across-strike profiles
247 through the entire fissure swarm (numbered 0-70 in Fig. 3). Figure 9 shows ten characteristic
248 profiles. We calculated elevations every meter along each profile. Outliers were removed
249 from the raw results according to two criteria. First, we removed outliers for which the value
250 of the local correlation parameter between the two images for each point was less than 0.5.
251 Second, we used a moving average filter on the nearest 24 points to remove elevations that
252 differed by more than 5 m. Even after this filtering, the elevation signal was still quite noisy.

253 As the amplitude of the noise was around 1 m, some normal faults with vertical throws of less
254 than 2 m may not have been distinguishable from the background noise. Taking into account
255 the uncertainties of the calculation method, we obtained a mean throw of 8-10 m for the main
256 faults (Fig. 9).

257 In the south of the network, the profiles clearly show that the lava flows dip gently
258 (~3%) to the NW. This surface dip decreases progressively towards the north of the network.

259 Many faults display an obvious bulge on the surface of the lavas on the upthrown side
260 ~50 m from the fault scarp (e.g., R16 in Fig. 9 and detail in Fig. 9A and 9B).

261 In the south (sections 0-40, Fig. 3), the entire fissure swarm has a graben structure,
262 bounded to the northwest by the east-facing Hrafnagjá normal fault (R16). In places, this large
263 fault is associated with a secondary normal fault (e.g., R21 on profile 23, Fig. 9). To the
264 southeast, the graben is bounded by the west-facing Grindavikurgjá normal fault (R59. This
265 fault is not shown on the across-strike profiles because of correlation difficulties during the
266 automatic plotting due to the location of this fault on the edge of the photographs). Faulting
267 deformation between the two boundary faults is mainly accommodated by west-dipping
268 normal faults, especially R24, R28, R38 and R55 in the southern part of the fissure swarm
269 (Fig. 9). These sub-parallel normal fault scarps form a step pattern that is characteristic of the
270 southern part of the VFS (see also Fig. 4).

271 The pattern in the northern part of the VFS is slightly different, as there is no
272 equivalent of the Hrafnagjá fault, and the western part of the network is composed mostly of
273 fissures and minor faults. Consequently, the general structure changes to a hemi-graben,
274 bounded to the southeast by two major normal faults (Klefgjá and Grindavikurgjá, R48 and
275 R59, Fig. 9)

276 Some scarps along a single fault vary in shape. Generally, faults at the surface of the
277 VFS are characterized by a near-vertical fault plane (e.g., R16 A in Fig. 9, and Fig. 5) but in
278 some places the fault plane is flanked by a narrow monocline that, on the scale of our across-
279 strike profiles, appears as a smooth bulge (e.g., compare R28 D and C in Fig. 9; see also Grant
280 and Kattenhorn, 2004).

281 In this study, we decided not to focus on fault width (opening) for two reasons. (i) The
282 methodology we used did not allow us to measure small widths, thereby precluding an
283 exhaustive analysis. (ii) The true width is often less than the measured width due to the
284 existence of graben-like structures. Despite the uncertainties caused by this overestimation of

285 some of the widths, Guðmundsson (1987a) produced some accurate width measurements in
286 the VFS (1076 points measured) along six main fractures (R16, R24, R28, R38, R55 and R67
287 in the present study). He obtained a mean width for all the points measured of 0.6 m and an
288 absolute maximum width for a single fracture of 7.5 m.

289 *4.6 Changes in along-strike fault throws for the main composite fractures*

290 We also produced automatic plots of along-strike profiles (see section 3) for five main
291 composite fractures: the east-facing fracture (R16) that forms the western boundary of the
292 VFS and four west-facing fractures (R24, R28, R38 and R48) within the fissure swarm (see
293 Fig. 3 for locations). For each main composite fracture, we started with the central trace (axis
294 of the fractured strip) and calculated two sets of two parallel traces, 20 m and 40 m from the
295 main scarp, on the hanging wall and on the footwall, respectively. The mean distance between
296 points was ~5 m. We then used the automatic image correlator to calculate the elevation of
297 each point on all the traces.

298 Each of the four profiles for a given fracture has the same number of points. The four
299 points with the same index on each profile represent a cross-section of the fracture and the
300 differences in their elevations correspond to the vertical throw at distances of 20 m and 40 m
301 from the main scarp. The profiles in Figure 10 show along-strike variations in these
302 differences, that is, changes in the vertical throw.

303 Main composite fracture R16 (Hrafnagjá) is fully visible over a distance of 2500 m.
304 The profiles show that the throw is greatest in the central part of the fault and decreases
305 towards its tips. This fault forms the western boundary of the VFS. Its maximum throw is ~10
306 m.

307 The other four normal main composite fractures we analyzed are located between the
308 two main boundary faults and are all west facing. They range in length from 2800 m to 5400
309 m, but the Skógfellahraun aa lava flow covers the southwestern ends of three of these
310 fractures (R24, R28, R38).

311 Main composite fracture R48 (Kvelfgjá) is 5400 m long and is visible in its entirety.
312 Its profile consists of three similar, 1500-2000 m long segments, each of which is similar in
313 size and shape to fault R16. Each segment has a mean maximum throw of 8-10 m in its
314 central part. This throw decreases to zero at the segment tips. A second periodicity, with an
315 amplitude of 2-4 m, modulates the profile of each segment every 250-500 m.

316 Main composite fracture R38 is visible over a distance of ~2800 m. It has a maximum
317 throw of 11.5 m and the throw decreases towards the northeast. The throw decreases ~1000 m
318 from the trace, corresponding to the junction with another main composite fracture (R36 in
319 Fig. 3 and Fig. 11). To the southeast, fractures R36 and R38 are parallel to each other and
320 each fracture probably accommodates part of the deformation.

321 Main composite fracture R28 is 3500 m long and has a maximum throw of ~10 m. As
322 for main composite fracture R48, the profile is modulated by a ~500-m periodicity with an
323 amplitude of ~5 m. The throw decreases in four places along the profile where the fracture is
324 mostly composed of fissures, rather than normal faults.

325 Main composite fracture R24 is 3000 m long. Again, it has a maximum throw of ~10
326 m but there is no variation in the throw along a significant part of the profile. Then, the throw
327 decreases steadily to the northwest over the last 500 m.

328 Compared with the throw profiles for complete fractures R16 and R48, it is evident
329 that the southeastward decrease in throw is missing from main composite fractures R24, R28
330 and R38. This decrease probably occurs in the part of the fractures in the aa lava flow. The
331 total length of these faults could not be measured.

332 In general, the throws calculated from the profiles 20-m and 40-m from the main scarp
333 have very similar shapes along the main composite fractures. The 20-m and 40-m throw
334 profiles for R28 and R38 are almost identical. The forms of the 20-m and 40-m profiles for
335 R48 are very similar, even in their minor variations (small peaks and troughs). The only
336 difference is the throw itself, as the throw 40 m from the main scarp is systematically smaller
337 (by 2-3 m on average) than the throw 20 m from the main scarp. The differences in the R16
338 and R24 profiles are greater, not only because the 40 m profile (for R24) has a systematically
339 smaller throw, but also because there are discrepancies between peaks and troughs (1.5 km
340 and 2 km from the southwestern tip for R16, and 0.5 km and 1.3 km from the southwestern tip
341 for R24). The differences between the 20-m and 40-m profiles are mainly due to the lava flow
342 almost systematically sticking up slightly on the upthrown side close to the fault scarp (Fig.
343 9). Local discrepancies, such as those shown by profiles R16 and R24, are due to the presence
344 of lava swells of volcanic origin.

345 *4.7 The linkage zones*

346 The main composite faults are composed of alignments of several individual fractures,
347 presenting different types of linkage at the surface. There are two main types of linkage

348 pattern: (i) a non-overlapping pattern with aligned or non-aligned segments, and (ii) an
349 overlapping pattern with fault segments that curve at their tips. The linkage of smaller
350 segments into larger segments allows the growing of faults and depend in detail of the
351 distances between their nearby tips relative to the segment lengths (Guðmundsson, 2011).

352 Although some neighboring aligned segments tend to propagate toward each other (Fig. 12a)
353 and a number of non-aligned segments are linked by en echelon or oblique fractures that
354 develop between fracture tips (Fig. 12b), most linkages form overlap patterns. We noted three
355 types of overlap feature. In some overlapping segments, the tips of one segment propagate to
356 the sidewall of another segment along a curved path (Fig. 12c). In other overlapping
357 segments, parallel en-echelon fractures develop in the linkage zone (Fig. 12f). The final type
358 consists of parallel fault segments that overlap over a long distance (Fig. 12e). Some linkage
359 zones are complex and can include, for example, oblique and parallel fractures (Fig. 12g) or a
360 horsetail feature (Fig. 12d, h).

361 In general, linkage zones connect the hanging wall of one fault to the footwall of
362 another fault and transfer the displacement from one fault to the other. For both overlapping
363 and non-overlapping patterns, open fractures can develop in the linkage zone (Fig. 2, Fig.
364 12). Similar intermediate (or mixed) patterns to the ones we found in the VFS have also been
365 described in other Icelandic fissure swarms (Guðmundsson, 1987a, b; Acocella et al., 2000;
366 Grant and Kattenhorn, 2004; Tentler, 2005; Tentler and Mazzoli, 2005; Friese, 2008).

367 Topologically, junctions between fracture traces can be described as immature and
368 mature. In the immature state, it is possible to pass from one side of a fracture to the other
369 without crossing any visible fissure or fault. In the mature state, the two main segments are
370 completely connected and the two sides of the fault are totally separated; hence,
371 fragmentation is complete (Fig 13). Immature junctions are quite frequent along the main
372 composite fractures of the VFS.

373

374 **5. Discussion: formation and growth of fissures and normal faults**

375 In the VFS, the spatial distribution of faults and fissures, as well as the changes in fault
376 throws, allow investigating linkage and forward propagation models both vertically and
377 horizontally. They permit to highlight the process of fault segments coalescence and the
378 resulting changes in fault architecture.

379 *5.1 Surface deformation and structure at depth*

380 In the Icelandic crust, magma intrusion at depth is generally agreed to have a major
381 effect on the development of tectonic structures (e.g., Angelier et al., 1997). However, how
382 normal faults grow vertically is an important unanswered question. Evidence provided by
383 combining seismicity and magma accumulation data suggests that most normal faulting
384 occurs at depths of 1-5 km (Einarsson, 1991; Hreinsdóttir et al., 2001). A number of models
385 favor upward propagation from depth (Grant and Kattenhorn, 2004; Tentler, 2005), whereas
386 others promote downward propagation from the surface (Acocella et al., 2003). Others still
387 advocate sub-simultaneous downward and upward propagation (Guðmundsson, 1992; Martel
388 and Langley, 2006).

389 It has often been assumed that a single shear zone will usually be unable to grow in its
390 own plane and develop into a normal fault (e.g., Scholz, 2002). Guðmundsson (1992)
391 suggested two mechanisms for normal fault initiation: (i) nucleation from large-scale tension
392 fractures originating at the surface and propagating to significant crustal depths, and (ii)
393 nucleation on sets of en-echelon joints when lava flows become tilted. Guðmundsson
394 maintains that these two mechanisms can occur concurrently, with the upper part of a fault
395 nucleating on a large-scale tension fracture and the lower part nucleating on a set of inclined
396 joints. He also suggests that large-scale tension fractures change into normal faults when they
397 reach a critical depth that partly depends on the tensile strength of the host rock. Thus, a mean
398 tensile strength of 3 MPa (Haimson and Rummel, 1982) corresponds to a change at a crustal
399 depth of ~0.5 km. The critical crustal depth at which inclined joints start to link up into
400 normal faults, taking into account the associated friction, is ~0.8 km, and the process is
401 common at ~1.5 km (Guðmundsson, 1992). Given these two nucleation zones, Guðmundsson
402 concludes that normal faulting starts to nucleate at crustal depths of 0.5-1.5 km.

403 Following studies of the Krafla fissure swarm in northeast Iceland, Angelier et al.
404 (1997) and Dauteuil et al. (2001) put forward a comparable model to Guðmundsson's for the
405 relationships between open fracture geometry observed at the surface and normal fault dip
406 inferred at depth. In this model, normal shear also plays a major role at intermediate depths in
407 the upper brittle crust and normal faulting occurs along planes with a mean dip of 60-75° at a
408 crustal depth of ~1 km. No hypotheses for the growth mechanism were put forward.

409 Many studies have compared dike and fissure swarms, suggesting or refuting strong
410 links between faults and fissures at the surface of active zones and deep dyke swarms
411 (Helgason and Zentilli, 1985; Forslund and Guðmundsson, 1991; Guðmundsson, 1995a, b,
412 2003; Tentler, 2005; Paquet et al, 2007). Some authors (e.g., Rowland et al., 2007, in the Afar

413 rift) assume (i) that normal faults are initiated or reactivated ahead of and above propagating
414 dyke and (ii) that preexisting subvertical cooling joints are reactivated as opening mode
415 fissures above the upper tip line of the normal faults. In such case the horizontal segmentation
416 of the main fault traces observed every 500-1500 m in our study (Fig. 10) could have
417 originated either via irregularities in the shape of the dike or via a segmentation of the dike
418 itself, which is a common feature in dike patterns (e.g., Guðmundsson, 2002). However, other
419 authors, based on field comparisons between dyke swarms and fault patterns in the eroded
420 palaeo-rift zones, demonstrated that the number of dykes by far exceeds the number of normal
421 faults in the same sections and even that where the dyke frequency was high, the fault
422 frequency was low (e.g., Forslund and Guðmundsson, 1991; Guðmundsson, 2003; Paquet et
423 al., 2007).

424 *5.2 Segmentation and changes in the throw and length of the fault traces*

425 Cowie and Roberts' (2001) conceptual model of fault growth shows how a set of faults
426 connected at their tips evolves into a single fracture. Applied to the longitudinal profiles
427 shown in Figure 10, this model can be used to interpret the different stages we observed.
428 Cowie and Roberts distinguish two main stages (Fig. 14) in the growth of faults: a first stage
429 of isolated growth during which the throw increases moderately compared to the length,
430 followed by a second stage, when the segments are connected, during which there is a large
431 increase in the throw but only a small (or no) increase in length.

432 Cowie and Roberts (2001) identified two ways in which this second stage can proceed,
433 depending on whether or not the faults are strongly interconnected. When the links between
434 the faults are weak, the junctions between the segments become complete at the end of the
435 process, after the central parts have stopped growing. When the links between the faults are
436 strong, the throw gradually increases everywhere and the distinctions between the segments
437 gradually disappear. Our data show situations that may indicate a third, intermediate way for
438 this stage to proceed (Fig. 14). Once the segments are connected, we observed an initial step
439 (P1) during which the throw increases more in the central part of the segments than at the
440 junctions, where the throw remains small. This is followed by a second step (P2) during
441 which the throw differences at the junctions disappear.

442 Considered as a whole, R48 (Fig. 10) is an example of a fault at the end of stage 1
443 (Fig. 14), at which point the three segments are connected. In the following step, the throw of
444 the central segment should increase more than the throw in the other two segments. Finally,

445 the differences in the throws of the segments should decrease until the fault achieves an
446 elliptical profile encompassing the three segments.

447 Analysis of the individual segments of faults R28 and R48 (Fig. 10) suggests that the
448 process is more advanced than in the case of fault R48 taken as a whole. For all the segments,
449 the throw differences at the tips of the initial segments are being reduced and the general
450 profile is elliptical. It should be noted that the initial segments of fault R48 are ~250 m long,
451 whereas the typical length of the segments of R28 is 500 m.

452 According to the conceptual model, fault R16 corresponds to the final stage in the
453 process, when any individual segments that existed at the beginning of fault development
454 have become indistinguishable.

455 *5.3 Limitation of the throw and maximum throw/length ratio*

456 The throws we measured in the VFS are significantly smaller than the throws
457 measured in other Icelandic fissure swarms in lava flows of comparable age (Opheim and
458 Guðmundsson, 1989; Dauteuil et al. 2001; Tentler and Mazzoli, 2005, Sonnette et al., 2010).
459 In addition, maximum throws in the VFS are very similar between the different faults, often
460 ~10 m. In other areas, maximum throws have been found to be related to the length of the
461 faults by a power law (Sonnette et al., 2010).

462 Compared with previously published data (Gupta and Scholz, 2000), the maximum
463 throw/fault-length ratio is small. Considering the 2-km segments along fault R48 to be single
464 faults gives a maximum throw/fault-length ratio of 0.005, which is four times smaller than the
465 mean ratio reported by Gupta and Scholz (2000). Consequently, the throws of the segments
466 we measured are likely to increase without the segments necessarily increasing in length.

467 *5.4 Interaction and linkage of fissures and normal faults*

468 As mentioned in section 4.7, interaction and linkage zones occur in all Icelandic
469 fissure swarms. Linkage zones have been described in similar basaltic rocks in other
470 geodynamic contexts, such as Kilauea Volcano in Hawaii (Peacock and Parfitt, 2002; Martell
471 and Langley, 2006), as well as in many other geological settings and rock types, especially
472 since the early 1990s (e.g., Morley et al., 1990; dePolo et al., 1991; Peacock and Sanderson,
473 1991; Anders and Schlische, 1994; Gupta and Scholz, 2000; Marchal et al., 2003).

474 In the case of the VFS, most of the links between faults are marked by an overlap
475 zone, with direct connections between segments occurring in only a few cases of closely

476 aligned segments (e.g., Fig. 12b). As described in section 4.7, most of the VFS links are of
477 immature type (connection not complete at the surface). Detailed examination of the topology
478 of overlapping areas reveals a predominance of left stepping *en-echelon* ruptures. This may
479 indicate a small strike-slip component in addition to the main normal movement, which is
480 consistent with the general behavior of the area as a large, left-lateral shear zone, either
481 partitioned into NE-SW *en-echelon* fracture zones (Clifton et al., 2003), or resembling a
482 transtensional segmented transform, as suggested by Geoffroy et al. (2008).

483 *5.5 Spacing of main composite fractures and thickness of layers*

484 It should be noted that the general structure of the VFS is not that of a typical graben.
485 The structure is not axially symmetrical, as the front of the faults in the southeast is not
486 opposite the front of the faults in the northwest, except in the case of fault R16 (Fig. 2 and 9).
487 The cross-sections (Fig. 9) show four or five major faults, and the boundary and central faults
488 have similar throws. The spacing of parallel main composite fractures contains at least two
489 modes at 225 m and 450 m (Fig. 8). It should be noted that spacing of large fault zones in
490 Holocene Icelandic fissure swarms is very variable (e.g., Guðmundsson, 1987a,b; Opheim
491 and Guðmundsson, 1989), suggesting that the fault spacing may change during the lifetime of
492 a fissure swarm (Forslund and Guðmundsson, 1991).

493 The relationship between the spacing of the fracture zones and the thickness of the
494 brittle behavior levels has already been noted (e.g., Bai and Pollard, 2000; Ackermann et al.,
495 2001). Seismicity in our study area appears to be restricted to depths of less than 7-8 km, with
496 most earthquakes occurring at 4-6 km (Keiding et al., 2008). These values are too high to be
497 related directly to the observed spacing; however, they are similar to the total width of the
498 fissure swarm.

499 Grant and Kattenhorn (2004) modeled normal faulting ending at depths of 250 and
500 500 m, and extending to the surface along vertical fractures. They interpreted these structures
501 as ancient faults affecting deep layers that have subsequently been covered by younger lava
502 flows. Reactivation of these faults could lead to the development of vertical extensions. Grant
503 and Kattenhorn noted the presence of major discontinuities at depths of 250 and 500 m, which
504 could be the cause of mechanical decoupling. Another possibility, related to the potential
505 control of the geometry and development of the fault patterns by dykes is that the spacing of
506 the major fault zones reflects the spacing between the underlying dikes. This is however
507 unlikely in so far as some field studies (see section 5.1) have demonstrated that there is no
508 systematic relationship between fault and dyke swarms. Finally, it is also possible that the

509 different modes corresponds to different causes, including a mechanical decoupling and also
510 possibly reflecting the intrinsic mechanical properties of the upper levels of the brittle crust.

511

512 **6. Conclusion**

513 (1) Advanced photogrammetric techniques allowed us to accurately map the VFS and
514 differentiate between fissures and faults. We measured the throws of vertical faults with
515 throws greater than 0.5 m along five of the main fracture zones. By using remote sensing
516 methods we were able to carry out a comprehensive study of the area much more quickly than
517 would have been possible if we had relied solely on field measurements.

518 (2) The fracturing of the VFS includes both fissures (without vertical throw) and normal
519 faults (with vertical throw), both of which are generally accompanied by opening (from
520 several millimeters to several meters). Most of the fractures are grouped together into main
521 composite lines that generally include both fissures and normal faults. Seven of the normal
522 fault lines are longer than 2500 m. They mostly correspond to the main fault scarps of the
523 fissure swarm. The maximum throw is ~10 m and seems to be independent of the total length
524 of the fault.

525 (3) The VFS is an uncommon graben-like structure, bounded to the east and to the west by
526 major normal faults that face west and east, respectively. Faulting deformation between the
527 two boundary faults is mostly accommodated by regularly spaced, west-dipping normal faults.
528 The throws of the boundary and inner faults are not significantly different.

529 (4) The structure of the fault zone may be closely linked to the network of underlying dikes.
530 When stopped in their progression toward the surface, these dikes may extend upwards as
531 normal faults, which will therefore show similar spacing to the dikes.

532 (5) In the throw profiles along the fully visible major normal faults, throws are biggest in the
533 central part of the fault segments and decrease towards the segment tips. Composite faults
534 contain several segments. The boundaries between the different segments remain visible for
535 almost the whole growth period.

536 (6) Detailed analysis of the throw profiles revealed different steps in the fault growth process.
537 The first step is characterized by a moderate increase in throw compared to the increase in
538 length, whereas the second step involves an increase in throw with no or very little increase in
539 length.

540 (7) The faults in the VFS appear to be very long compared to their throws, suggesting that
541 they may be immature faults with a high potential for further growth. Given the current
542 lengths of the faults, their throws could be expected to increase 3-5 fold without significant
543 lengthening.

544 (8) Analysis of the linkage zones between fault segments revealed a slight but systematic
545 shearing component. This is consistent with the general transform behavior of the Reykjanes
546 Peninsula.

547

548 **Acknowledgements**

549 We thank Yves Egels for allowing us to use his Poivilliers software for the stereoscopic
550 analysis. Jacques Angelier, Olivier Dauteuil and Guillaume Biessy helped with GCP
551 acquisition. Jacques Angelier also assisted with the production of the photo-mosaics and
552 provided encouragement during the initial stages of the study. We are grateful to Alexandre
553 Lethiers (ISTeP) and André Paillet (Edytem) for their help in drawing the figures. We thank
554 Paul Henderson who read the manuscript and significantly improved our English writing.
555 Águst Guðmundsson and Valerio Acocella are thanked for their helpful reviews and
556 comments. Financial support was provided by the French Polar Institute (IPEV) via Arctic
557 Program 316 IPCROCI.

558

559 **References**

- 560 Ackermann, R.W., Schlische, R.W., Withjack, M.O., 2001. The geometric and statistical
561 evolution of normal fault systems: an experimental study of the effects of mechanical layer
562 thickness on scaling laws. *Journal of Structural Geology* 23, 1803-1819.
- 563 Acocella, V., Guðmundsson, Á., Funicello, R., 2000. Interaction and linkage of extension
564 fractures and normal faults: examples from the rift zone of Iceland. *Journal of Structural*
565 *Geology* 22, 1233-1246.
- 566 Acocella, V., Korme, T., Salvini, F., 2003. Formation of normal faults along the axial zone of
567 the Ethiopian Rift. *Journal of Structural Geology* 25, 503-513.
- 568 Anders, M.H., Schlische, R.W., 1994. Overlapping faults, intra-basin highs, and the growth of
569 normal faults. *Journal of Geology* 102, 165-180.

- 570 Angelier, J., Bergerat, F., Dauteuil, O., Villemin, T., 1997. Effective tension-shear
571 relationships in extensional fissure swarms, axial rift zone of northeastern Iceland. *Journal*
572 *of Structural Geology* 19, 673-685.
- 573 Árnadóttir, Th., Geirsson, H., Jiang, W., 2008. Crustal deformation in Iceland: Plate spreading
574 and earthquake deformation. *Jökull* 58, 59-74.
- 575 Bai, T., Pollard, D.D., 2000. Fracture spacing in layered rocks: a new explanation based on
576 the stress transition. *Journal of Structural Geology* 22, 43-57.
- 577 Cartwright, J.A., Trudgill, B.D., Mansfield, C.S., 1995. Fault growth by segment linkage: an
578 explanation for scatter in maximum displacement and trace length data from the
579 Canyonlands Grabens of SE Utah. *Journal of Structural Geology* 17, 1319-1326.
- 580 Childs, C., Watterson, J., Walsh, J.J., 1995. Fault overlap zones within developing normal
581 fault systems. *Journal Geological Society London* 152, 535-549.
- 582 Childs, C., Nicol, A., Walsh, J.J., Watterson, J., 1996. Growth of vertically segmented normal
583 faults. *Journal of Structural Geology* 18, 1389-1397.
- 584 Clifton, A.E., Kattenhorn, S.A., 2006. Structural architecture of a highly oblique divergent
585 plate boundary segment. *Tectonophysics* 419, 27-40.
- 586 Clifton, A.E., Pagli, C., Jónsdóttir, J.F., Eythorsdóttir, K., Vogfjörð, K., 2003. Surface effects
587 of triggered fault slip on Reykjanes Peninsula, SW Iceland. *Tectonophysics* 369, 145-154.
- 588 Cowie, P.A., Knipe, R.J., Main, I.G., 1996. Introduction to the special issue: Scaling laws for
589 fault and fracture populations, analyses and applications. *Journal of Structural Geology* 18,
590 v-xi.
- 591 Cowie, P.A., Roberts, G.P., 2001. Constraining slip rates and spacings for active normal
592 faults. *Journal of Structural Geology* 23, 1901-1915.
- 593 Dauteuil, O., Angelier, J., Bergerat, F., Verrier, S., Villemin, T., 2001. Deformation
594 partitioning inside a fissure swarm of the northern Icelandic rift. *Journal of Structural*
595 *Geology* 23, 1359-1372.
- 596 dePolo, C.M., Clark, G.C., Slemmons, D.B., Ramelli, A.R., 1991. Historical surface faulting
597 in the Basin and Range province, western North America: implications for fault
598 segmentation. *Journal of Structural Geology* 13, 123-136.

- 599 DeMets, C., Gordon, R.G., Argus, F., Stein, S., 1990. Current plate motions. *Geophysical*
600 *Journal International* 101, 425-478.
- 601 DeMets, C., Gordon, R.G., Argus, F., Stein, S., 1994. Effect of recent revisions to the
602 geomagnetic reversal time scale on estimates of current plate motions. *Geophysical*
603 *Research Letters* 21, 2191-2194.
- 604 Einarsson, P., 1991. Earthquakes and present-day tectonism in Iceland. *Tectonophysics* 189,
605 261-279.
- 606 Forslund, T., Guðmundsson, A., 1991. Crustal spreading due to dikes and faults in southwest
607 Iceland. *Journal of Structural Geology* 13, 443-457.
- 608 Friese, N., 2008. Brittle tectonics of the Thingvellir and Hengill volcanic systems, Southwest
609 Iceland: field studies and numerical modelling. *Geodinamica Acta* 21, 169-185.
- 610 Geoffroy, L., Dorbath, C., 2008. Deep downward fluid percolation driven by localized crust
611 dilatation in Iceland. *Geophysical Research Letters* 35, L17302,
612 doi:10.1029/2008GL034514.
- 613 Grant, J.V., Kattenhorn, S.A., 2004. Evolution of vertical faults at an extensional plate
614 boundary, Southwest Iceland. *Journal of Structural Geology* 26, 537-557.
- 615 Guðmundsson, Á., 1980. The Vogar fissure swarm, Reykjanes peninsula, SW Iceland. *Jökull*
616 30, 43-64.
- 617 Guðmundsson Á., 1986. Mechanical Aspects of Postglacial Volcanism and Tectonics of the
618 Reykjanes Peninsula, Southwest Iceland. *Journal of Geophysical Research* 91, 12711-
619 12721
- 620 Guðmundsson, Á., 1987a. Geometry, formation and development of tectonic fractures on the
621 Reykjanes Peninsula, Southwest Iceland. *Tectonophysics* 139, 295-308.
- 622 Guðmundsson, Á., 1987b. Tectonics of the Thingvellir Fissure Swarm, SW Iceland. *Journal*
623 *of Structural Geology* 9, 61-69.
- 624 Guðmundsson, Á., 1992. Formation and growth of normal faults at the divergent plate
625 boundary in Iceland. *Terra Nova* 4, 464-471.
- 626 Guðmundsson, Á., 1995a. The geometry and growth of dikes. In: Baer, G., Heimann, A.
627 (Eds.), *Physics and Chemistry of Dikes*. Balkema, Rotterdam, 23-34.

- 628 Guðmundsson, Á., 1995b. Infrastructure and mechanisms of volcanic systems in Iceland.
629 *Journal of Volcanology and Geothermal Research* 64, 1-22
- 630 Guðmundsson, Á., 2002. Emplacement and arrest of sheets and dikes in central volcanoes.
631 *Journal of Volcanology and Geothermal Research*, 116, 279-298.
- 632 Guðmundsson, Á., 2003. Surface stresses associated with arrested dykes in rift zones.
633 *Bulletin of Volcanology* 65, 606-618.
- 634 Guðmundsson, Á., 2011. Rock fractures in geological processes. Cambridge University
635 Press, 578 p.
- 636 Guðmundsson, Á., Bäckström K., 1991. Structure and development of the Sveinagjá graben,
637 Northeast Iceland. *Tectonophysics* 200, 111-125.
- 638 Gupta, A., Scholz, C.H., 2000. A model of normal fault interaction based on observations and
639 theory. *Journal of Structural Geology* 22, 865-879.
- 640 Haimson, B.C., Rummel, F., 1982. Hydrofracturing stress measurements in the Iceland
641 research drilling project drill hole at Reyðarfjörður, Iceland. *Journal of Geophysical*
642 *Research* 87, 6631-6649.
- 643 Helgason, J., Zentilli, M., 1985. Field characteristics of laterally emplaced dikes: anatomy of
644 an exhumed Miocene dike swarm in Reyðarfjörður, eastern Iceland. *Tectonophysics* 115,
645 247-274.
- 646 Hjartardóttir, Á. R., Einarsson, P., Sigurdsson, H., 2009. The fissure swarm of the Askja
647 volcanic system along the divergent plate boundary of N Iceland. *Bulletin Volcanology* 71,
648 961-975.
- 649 Hreinsdóttir, S., Einarsson, P., Sigmundsson, F., 2001. Crustal deformation at the oblique
650 spreading Reykjanes Peninsula, SW Iceland: GPS measurements from 1993 to 1998.
651 *Journal of Geophysical Research* 106, 13803-13816.
- 652 Huggins, P., Watterson, J., Walsh, J.J., Childs, C., 1995. Relay zone geometry and
653 displacement transfer between normal faults recorded in coal-mine plans. *Journal of*
654 *Structural Geology* 17, 1741-1755.
- 655 Jóhannesson, H., Sæmundsson, K., 2009. Geological map of Iceland, *Bedrock Geology*.
656 Icelandic Institute of Natural History, Reykjavik, 1st ed., scale 1:600 000.
- 657 Kasser, M., Egels, Y., 2001. Digital photogrammetry. Taylor and Francis, London.

- 658 Keiding, M., Árnadóttir, T., Sturkell, E., Geirsson, H., Lund, B., 2008. Strain accumulation
659 along an oblique plate boundary: The Reykjanes Peninsula, southwest Iceland, *Geophysical*
660 *Journal International* 172, 861 – 872, doi:10.1111/j.1365–246X.2007.03655.x.
- 661 Keiding, M., Lund, B., Árnadóttir, T., 2009. Earthquakes, stress and strain along an obliquely
662 divergent plate boundary: the Reykjanes Peninsula, southwest Iceland, *Journal of*
663 *Geophysical Research* 114, 861-872, B09306, doi: 10.1029/2008JB006253.
- 664 Mansfield, C. S., Cartwright, J. A., 1996. High resolution fault displacement mapping from
665 three-dimensional seismic data: evidence for dip linkage during fault growth. *Journal of*
666 *Structural Geology* 18, 249-263.
- 667 Marchal, D., Guiraud, M., Rives, T., 2003. Geometric and morphologic evolution of normal
668 fault planes and traces from 2-D to 4-D data. *Journal of Structural Geology* 25, 135-158.
- 669 Martel, S.J., Langley, J.S., 2006. Propagation of normal faults to the surface in basalt, Koaie
670 fault system, Hawaii. *Journal of Structural Geology* 28, 2123-2143.
- 671 Morley, C.K., Nelson, R.A., Patton, T.L., Munn, S.G., 1990. Transfer zones in the East
672 African rift system and their relevance to hydrocarbon exploration in rifts. *Bulletin*
673 *American Association Petroleum Geology* 74, 1234-1253.
- 674 Opheim, J. A., Guðmundsson, Á., 1989. Formation and geometry of fractures, and related
675 volcanism, of the Krafla fissure swarm, northeast Iceland, *Bulletin of the Geological*
676 *Society of America*, 101, 1608-1622.
- 677 Papanikolaou, I.D., Roberts, G.P., 2007. Geometry, kinematics and deformation rates along
678 the active normal fault system in the southern Apennines: Implications for fault growth,
679 *Journal of Structural Geology* 29, 166-188, doi: 10.1016/j.jsg.2006.07.009.
- 680 Paquet, F., Dauteuil, O., Hallot, E., Moreau, F., 2007. Tectonics and magma dynamics
681 coupling in a dyke swarm of Iceland, *Journal of Structural Geology* 29, 1477-1493.
- 682 Peacock, D.C.P., 1991. Displacements and segment linkage in strike-slip fault zones. *Journal*
683 *of Structural Geology* 13, 721-733.
- 684 Peacock, D.C.P., Parfitt, E.A., 2002. Active relay ramps and normal fault propagation on
685 Kilauea Volcano, Hawaii. *Journal of Structural Geology* 24, 729-742.
- 686 Peacock, D.C.P., Zhang, X., 1993. Field examples and numerical modeling of oversteps and
687 bends along normal faults in cross-section. *Tectonophysics* 234, 147-167.

- 688 Peacock, D.C.P., Sanderson D.J., 1991, Displacements, segment linkage and relay ramps in
689 normal fault zones. *Journal of Structural Geology* 13, 721-733.
- 690 Roberts, G.P., Michetti, A.M., 2004. Spatial and temporal variations in growth rates along
691 active normal fault systems: an example from The Lazio–Abruzzo Apennines, central Italy.
692 *Journal of Structural Geology* 26, 339–376.
- 693 Rowland, J. V., Baker, E., Ebinger, C. J., Keir, D., Kidane, T., Biggs, J., Hayward, N.,
694 Wright, T. J., 2007. Fault growth at a nascent slow-spreading ridge: 2005 Dabbahu rifting
695 episode, Afar. *Geophysical Journal International* 171, 3, 1226–1246.
- 696 Sæmundsson, K., 1978. Fissure swarms and central volcanoes of the neovolcanic zones in
697 Iceland. In : Bowes, D.R., Leake, B.E. (Eds), *Crustal Evolution in Northwestern Britain and*
698 *Adjacent Regions. Geological Journal Special Issue* 10, 415-432.
- 699 Sæmundsson, K., 1979. Outline of the geology of Iceland. *Jökull* 29, 7-28.
- 700 Sæmundsson, K., 1992. Geology of the Thingvallavatn area. *Oikos* 64, 40-68.
- 701 Scholz, C. H., 2002. *The Mechanics of Earthquakes and Faulting*, Cambridge Univ. Press,
702 New York.
- 703 Schöpfer, M.P.J., Childs, C., Walsh, J.J., 2006. Localisation of normal faults in multilayer
704 sequences. *Journal of Structural Geology* 28, 816-833.
- 705 Sonnette, L., Angelier, J., Villemin, T., Bergerat, F., 2010. Faulting and fissuring in active
706 oceanic rift: Surface expression, distribution and tectonic-volcanic interaction in the
707 Thingvellir Fissure Swarm, Iceland. *Journal of Structural Geology* 32, 407–422.
- 708 Tentler, T., 2005. Propagation of brittle failure triggered by magma in Iceland.
709 *Tectonophysics* 406, 17-38.
- 710 Tentler, T., Mazzoli, S., 2005. Architecture of normal faults in the rift zone of central north
711 Iceland. *Journal of Structural Geology* 27, 1721-1739.
- 712 Torabi, A., Berg, S.S., 2011. Scaling of fault attributes: A review. *Marine and Petroleum*
713 *Geology*, 28, 1444-1460.
- 714 Tryggvason, E., 1974. Vertical crustal movement in Iceland. In: Kristjanson, L. (ed),
715 *Geodynamics of Iceland and the North Atlantic Area*. Reidel, Dordrecht, 241-262.

716 Tryggvason, E., 1982. Recent ground deformation in continental and oceanic rift zones. In:
 717 Pálmason, G. (ed), Continental and Oceanic Rifts. AGU, Washington, Geodynamic Series
 718 8, 17-29.

719

720 **Figure captions**

721 Figure 1 - The Vogar Fissure Swarm (VFS) in southwest Iceland. A: The on-land
 722 neovolcanic rift in Iceland. The main fissure swarms are shown in grey. EVZ, NVZ and WVZ
 723 are the Eastern, Northern and Western Volcanic Zones, respectively. SISZ: South Iceland
 724 Seismic Zone. TFZ: Tjörnes Fracture Zone. V: Vatnajökull; B: Location of the four main
 725 fissure swarms in the Reykjanes Peninsula, H: Hengill central volcano. C: Schematic tectonic
 726 map of the Reykjanes fissure swarm. In light grey: Upper Pleistocene basic and intermediate
 727 hyaloclastites and lavas, younger than 0.8 m.yr. In white: Postglacial basic and intermediate
 728 lavas, older than AD 871. In dark grey: Postglacial basic and intermediate lavas, younger than
 729 AD 871, main normal faults are shown as thin lines with barbs. B and C modified after
 730 Sæmundsson (1979), Sæmundsson and Einarsson (1980), Guðmundsson (1986, 1987a), and
 731 Jóhannesson and Sæmundsson (2009).

732 Figure 2 - Aerial photograph mosaic of the VFS (photographs O8750, O8751 and
 733 O8752, 1998, from “Landmælingar Íslands”). All fractures identified in this study are shown
 734 as colored lines: East dipping normal faults in blue, with important opening shown in black;
 735 west dipping normal faults in green, with important opening shown in yellow; fissures (pure
 736 tension fracture) without vertical throw (or vertical throw smaller than 0.5 m) in red. Most of
 737 these fractures are concentrated within several fracture zones shown in Figure 3. Location
 738 grid uses UTM coordinates.

739 Figure 3 - Main composite fractures of the VFS and location of the along-strike and
 740 across-strike profiles. The thick grey lines are the main composite fractures; the black lines
 741 are fractures for which we plotted along-strike profiles. Numbers (R) refer to the main
 742 composite fractures described in the text. Small arrows numbered 0 to 70 indicate the
 743 locations of the across-strike profiles. Blue bands indicate the across-strike profiles shown in
 744 Figure 9. The red rectangle shows the location of Figure 11. Rose diagrams show the trends of
 745 the 156 individual faults and 322 individual fissures.

746 Figure 4 - West-facing, sub-parallel normal fault scarps illustrating the step pattern in
747 the VFS. A: Oblique aerial photograph taken from a helicopter (looking east), B: Detail of
748 two steps (looking southeast).

749 Figure 5 - A west-facing normal fault with opening in the VFS. The vertical throw is
750 ~ 2 m. Note the graben-like structure characteristic of near-surface normal faulting (i.e., fault
751 with both vertical and opening components).

752 Figure 6 - Fissures in the VFS. A: aerial photograph of a long fissure, taken from a
753 helicopter (looking northeast), B: fissure with a small vertical throw (smaller than 0.5 m)
754 observable near the photographer, C: detail of a small fissure opening; part of the fissure
755 follows the columnar joints yielding zigzag geometry.

756 Figure 7 - Distribution of fracture lengths. Histograms showing the number of
757 fractures (N) as a function of fracture length (L, in meters), with classes of 25 m for individual
758 fissures (A) and individual faults (B), and with classes of 250 m for main composite fractures
759 (C).

760 Figure 8 – Spacing of fractures in the VFS, with number of fractures (N) plotted as a
761 function of spacing (S, in meters). In blue (lozenges): All individual fractures (fissures and
762 faults). In red (squares): Individual fissures. In green (triangles): Main composite faults.

763 Figure 9 – Changes in the topography across the VFS. Sections 23-27 and 50-54 as
764 examples (see location in Figure 3). The number of main composite fractures cut by the
765 profiles is indicated. Lengths and altitudes are in meters. A-D profiles are enlargements of
766 fault scarps R16 and R28, which face east and west, respectively.

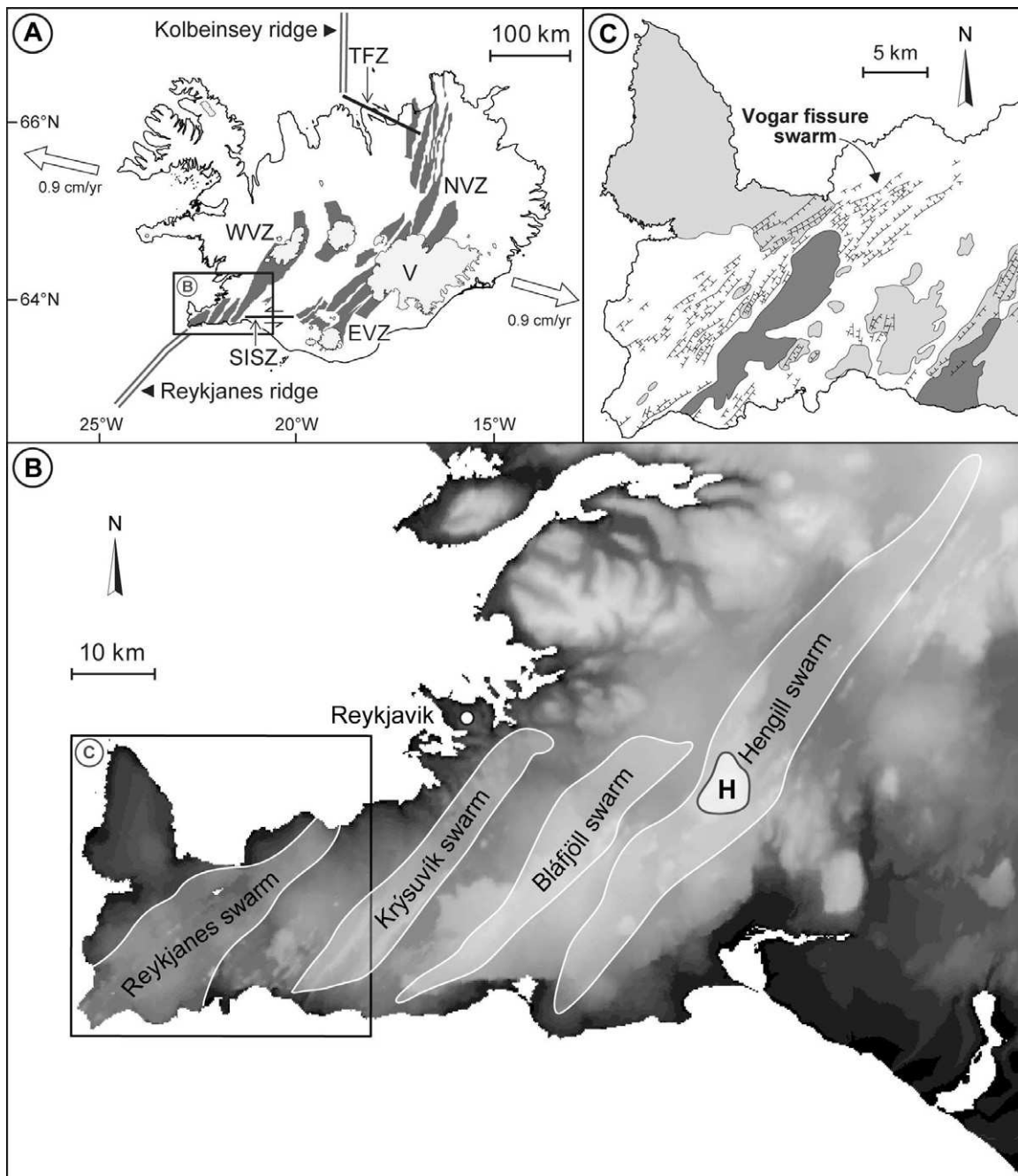
767 Figure 10 – Along-strike changes in fault throw for main composite fractures R16,
768 R24 R28, R38 and R48 (see location in Figure 3). All throws and distances are in meters.
769 Throw profile established from the along-strike topographic profiles at a distance of 20 m
770 from the main discontinuity are shown as black lines, and at a distance of 40 m are shown as
771 grey lines.

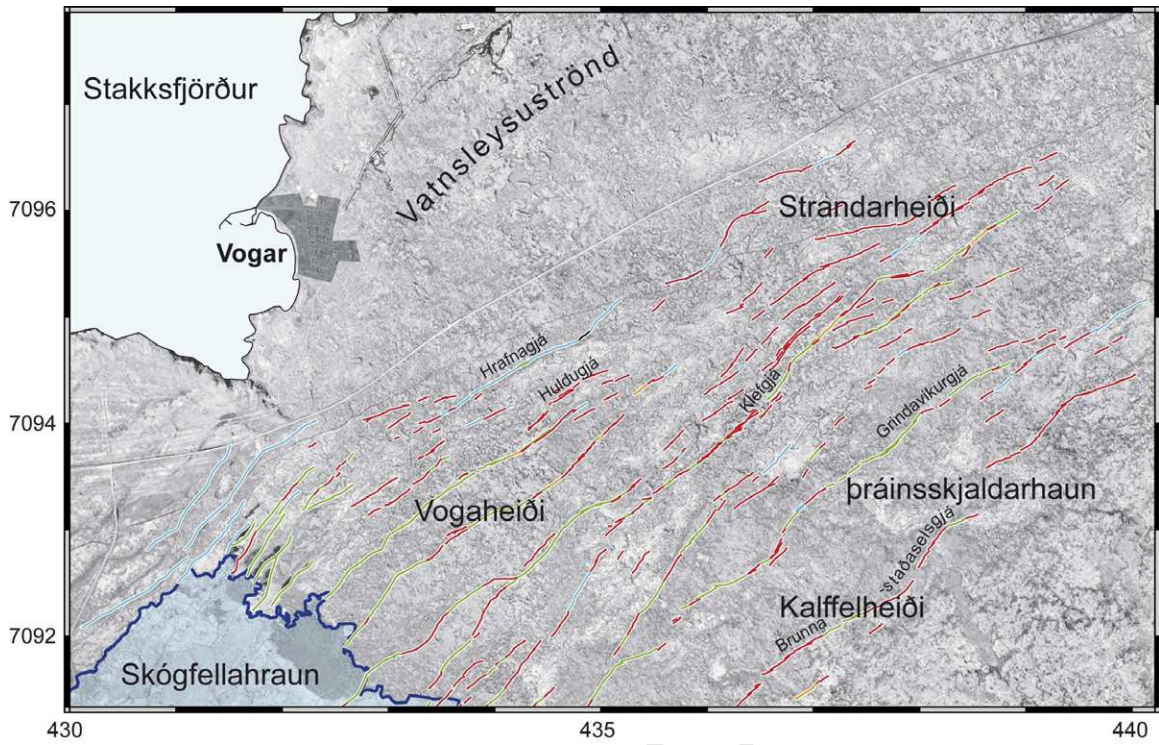
772 Figure 11 - Detailed view of the central part of fracture R38 and its junction with
773 fracture R36 (mosaic of a dozen oblique aerial photographs taken from a helicopter). Note the
774 smaller shadow of fault R38 in the left-hand two thirds of the mosaic, indicating a decrease in
775 its throw (here, the deformation is accommodated by R38 and by R36, which are parallel, see
776 location in Figure 3).

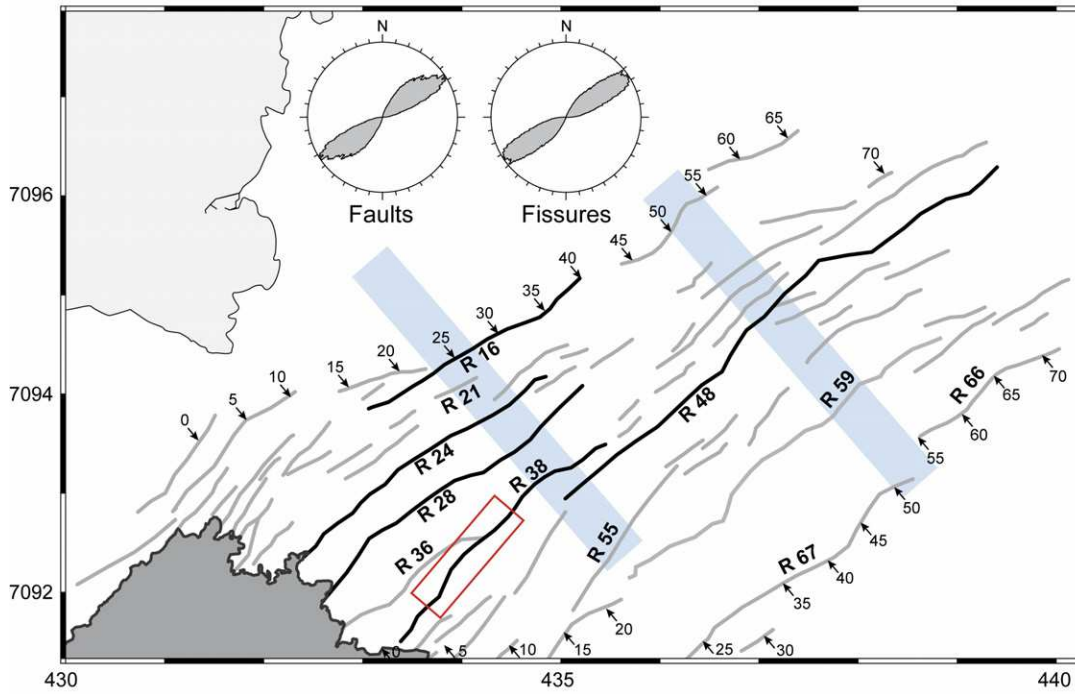
777 Figure 12 – Fault tips and fault linkages at the surface (aerial photographs taken from
778 a helicopter). (a) Non-overlapping close segments. (b) Non-overlapping segments with
779 oblique fracture forming the junction. (c) Poorly overlapping segments with each tip
780 propagating to the sidewall of the other segment. (d) Horsetail-type tip of a fault segment in
781 the linkage zone with another segment. (e) Amply overlapping sub-parallel close segments.
782 (f) Non-overlapping segment with sub-parallel en-echelon fractures forming the junction. (g)
783 Complex linkage zone including oblique and sub-parallel fractures. (h) Detail of the horsetail
784 tip of a fault.

785 Figure 13 – Immature and mature junctions between fault traces. It is possible to pass
786 from one side to the other of an immature fault without crossing any fractures (as shown by
787 the dotted line). In the mature state, the two fault segments are connected and the two sides of
788 the fault are fully separated.

789 Figure 14 – Conceptual model of fault growth in the VFS (adapted from Cowie and
790 Roberts, 2001; Roberts and Michetti, 2004; Papanikolaou and Roberts, 2007). (a) Model of
791 throw-fault length profile. Fault segments initially grow by increasing in length and in throw
792 (stage 1). At the end of stage 1, fault linkage occurs and fault segments interact over long
793 distances (stage 2). (b) Graph showing throw as a function of time for the central segment
794 shown in (a). This illustrates the throw enhancement rate as interaction and linkage proceed.
795 See text for a detailed explanation. SB: Segment boundary, d_1 : Maximum throw on each
796 segment prior to linkage, d_2 : Maximum throw on the entire fault after linkage, L_1 : Length of
797 a single segment, L_2 : Length of the fault after linkage.



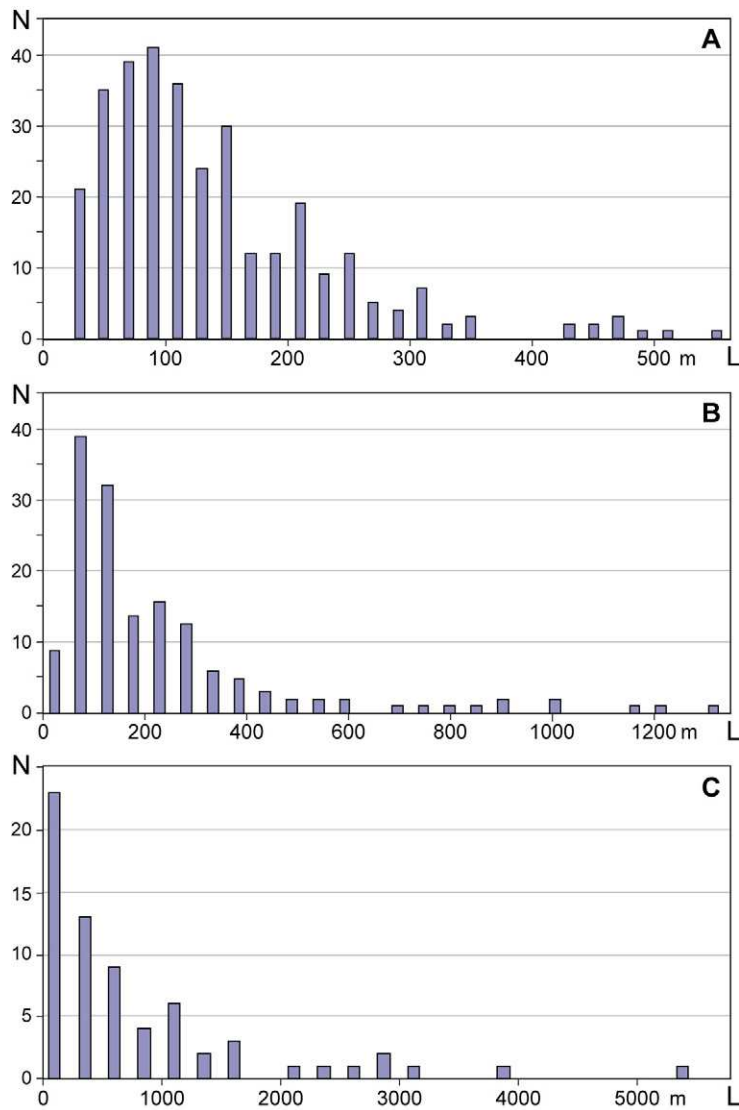


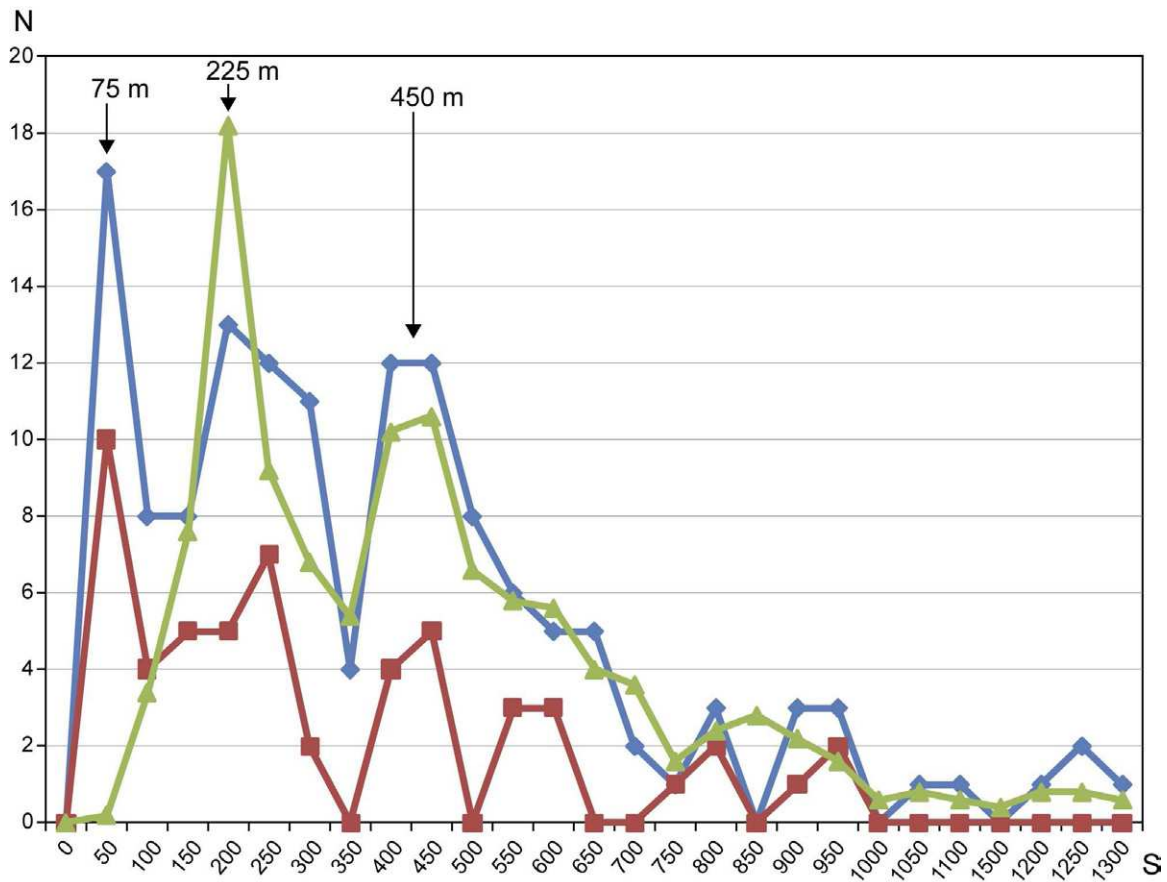


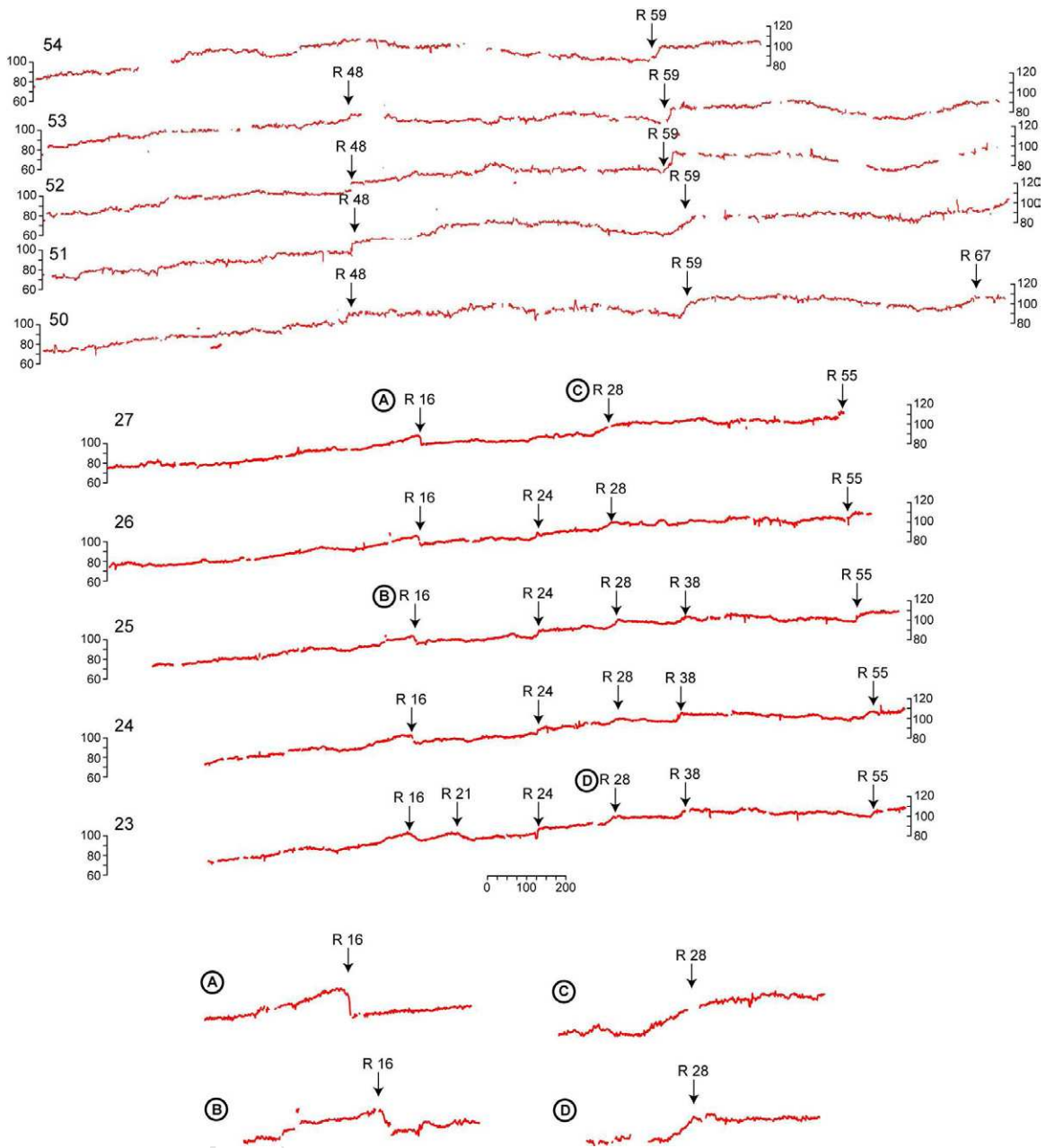


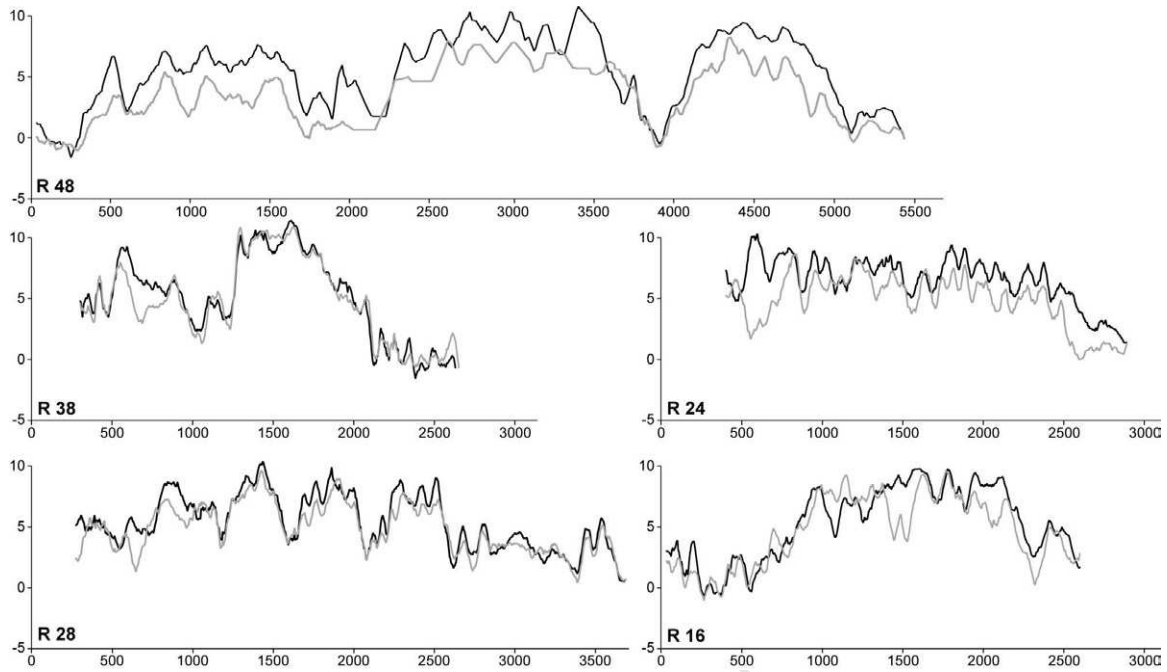




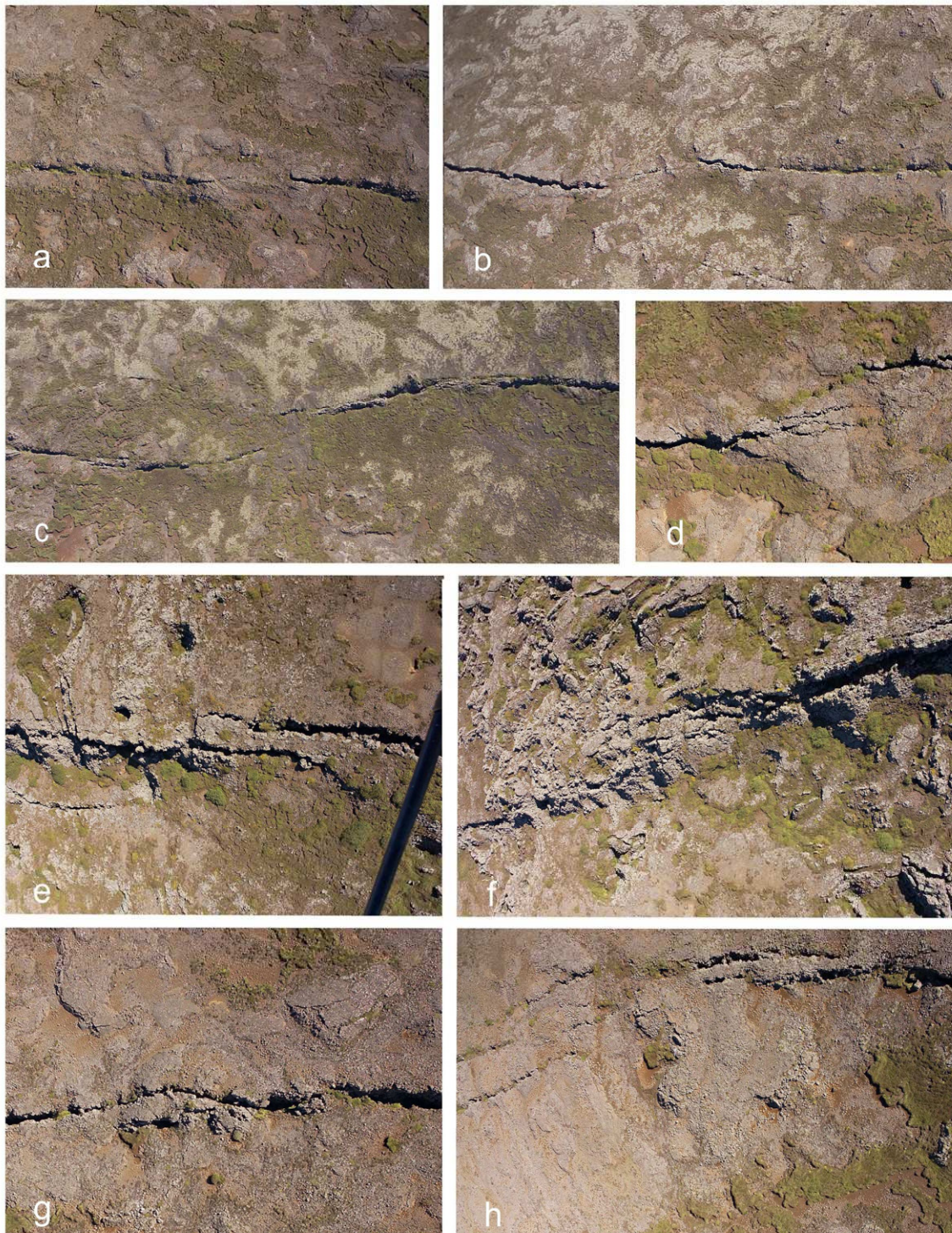


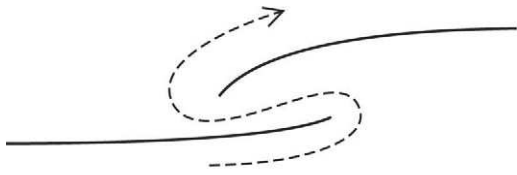












Immature stage



Mature stage

ACCEPTED MANUSCRIPT

